Available online at www.sciencedirect.com
ScienceDirect
International Journal of Heat and Mass Transfer 49 (2006) 4804–4820
International Journal of HEAT and MASS TRANSFER
www.elsevier.com/locate/ijhmt

A transient, multi-phase and multi-component model of a new passive DMFC

Jeremy Rice, Amir Faghri *

Department of Mechanical Engineering, University of Connecticut, 261 Glenbrook Road, Unit 2237, Storrs, CT 06269, United States

Received 1 April 2006; received in revised form 3 June 2006
Available online 10 August 2006

Abstract

A 2-dimensional, transient multi-phase, multi-component fuel cell model is developed to model a passive fuel delivery system including the fuel cell itself for a direct methanol fuel cell (DMFC). This model captures evaporative effects, as water and fuel management are crucial issues. The evaporation/condensation rates are formulated in a manner to capture non-equilibrium effects between the phases. Also, the full kinetics are modeled at both the anode and cathode catalyst layers, along with the electric potential of the membrane, catalyst and gas diffusion layers. The fuel cell operation is examined by quantifying the fuel consumption due to chemical reaction and evaporation as a function of feed concentration. The passive delivery system utilizes a porous media to passively deliver methanol to the fuel cell while controlling the concentration of methanol at the anode side to limit the amount of methanol cross-over. The results illustrate the feasibility of the passive thermal-management system, and characterize the relevant transport phenomena.

1. Introduction

Fuel cells are extensively being studied today because of their potential as an alternate energy source for a wide range of applications. Also, fuel cells are environmentally friendly. There are many unresolved issues in modeling and thermal/fuel management related to fuel cell technology. For a review on this subject, the authors refer to Faghri and Guo [1]. The DMFC is advantageous because of its low operating temperature and potential to store fuel in a liquid state; the operating temperature and fuel storage make it an excellent candidate for portable applications that run passively, i.e. without use of moving parts such as pumps, fans and blowers.

In a DMFC, the oxidation reaction mainly occurs at the anode catalyst layer, while the reduction reaction occurs at the cathode catalyst layer. The half reactions are

$$\text{Oxidation:}\quad CH_3OH + H_2O \overset{Pt/Ru}{\rightarrow} CO_2 + 6H^+ + 6e^-$$

$$\text{Reduction:}\quad \frac{3}{2}O_2 + 6H^+ + 6e^- \overset{Pt}{\rightarrow} 3H_2O$$

$$\text{Total:}\quad CH_3OH + \frac{3}{2}O_2 \rightarrow CO_2 + 2H_2O$$

Meyers and Newman [2] developed a kinetics model to describe the methanol oxidation on a Pt-Ru catalyst. Garcìa et al. [3] used a similar reaction mechanism as Meyers and Newman but did not segregate the electrochemical oxidation of water reaction from the electrochemical oxidation of CO. Their reaction mechanism assumes that the most significant reactions are the adsorption of methanol and the oxidation of CO. The kinetic expression of Meyers and Newman and of Garcìa et al. is not appreciably different because the oxidation of water on Ru occurs much fast than the oxidation of CO.

One of the serious problems with a DMFC is methanol crossover. Methanol crossover is when methanol crosses through the membrane and reacts at the cathode catalyst layer; the result is a reduction in cell power output and wasted fuel. Methanol crossover is caused by diffusion

* Corresponding author.
E-mail address: amir.faghri@uconn.edu (A. Faghri).

0017-9310/$ - see front matter © 2006 Elsevier Ltd. All rights reserved.
doi:10.1016/j.ijheatmasstransfer.2006.06.003

Nomenclature

A	area of fuel cell (m^2)
a	constant in coefficient matrix
a_{sf}	specific area (m^{-1})
a_{ox}	specific area for oxidation (m^{-1})
a_{red}	specific area for reduction (m^{-1})
b	element in solution matrix
$\mathbf{B}$	coefficient matrix for Stefan–Maxwell (s/m^2)
c_{MeOH}	methanol concentration in liquid (mol/cm^3)
c_{H_2O}	water concentration in liquid (mol/cm^3)
d_g	characteristic length of gas phase (m)
D_{ij}	binary diffusivity (m^2/s)
$D_{eff,ij}$	effective diffusivity of gas phase (m^2/s)
F	Faraday constant (C/mol)
h_{fg}	latent heat of vaporization (J/kg)
h_m	mass transfer coefficient (ms)
$I_{0,ref}^{MeOH}$	oxidation exchange current density (A/m^2)
$I_{0,ref}^{O_2}$	reduction exchange current density (A/m^2)
$\mathbf{I}$	current density (A/m^2)
$\mathbf{I}_p$	proton current density ($proton/m^2\ s$)
$\mathbf{J}$	mass flux ($kg/m^2\ s$)
$J(s)$	Leverette function
k_{rg}	relative permeability of gas phase
k_{rl}	relative permeability of liquid phase
$\mathbf{K}$	Permeability (m^{-2})
$\dot{m}'''$	mass source ($kg/m^3\ s$)
M_i	molecular weight of component i (kg/mol)
M_g	molecular weight of gas (kg/mol)
M_l	molecular weight of liquid (kg/mol)
$\mathbf{n}$	surface normal vector
n_d	electro-osmotic drag coeff. (mol/mol)
p_c	capillary pressure (Pa)
p_l	liquid pressure (Pa)
p_g	gas pressure (Pa)
R_u	ideal gas constant (J/mol K)
R_Ω	resistance (Ω)
R_{ox}	oxidation reaction rate (A/m^3)
R_{red}	reduction reaction rate (A/m^3)
Re_ε	pore Reynolds number
t	time (s)
T	temperature (K)
s	liquid saturation
$\mathbf{V}_k$	velocity of phase k (m/s)
$\langle\mathbf{V}_k\rangle^k$	intrinsic phase velocity of phase k (m/s)
V	volume (m^3)
x_{MeOH}	mole fraction of methanol in liquid (mol/mol)
x	distance in x-direction (m)
y	distance in y-direction (m)
α_l	liquid volume fraction
$\alpha_{l,MeOH}$	volume fraction of MeOH in liquid phase
α_a	anode transfer coefficient
α_c	cathode transfer coefficient
ε	porosity
η	fuel consumption efficiency
η_a	anodic overpotential (V)
η_c	cathodic overpotential (V)
λ	oxidation constant (mol/cm^3)
μ	viscosity (Ns/m^2)
θ	contact angle between liquid and solid (radians)
σ	surface tension (N/m)
σ_c	electrical conductivity of carbon phase ($\Omega^{-1}\ m^{-1}$)
σ_m	proton conductivity of membrane phase ($\Omega^{-1}\ m^{-1}$)
ρ	density (kg/m^3)
τ	tortuosity
$\omega_{g,i}$	mass fraction of gas (kg/kg)
$\omega_{g,i,sat}$	mass fraction of gas (kg/kg)
$\omega_{l,i}$	mass fraction of liquid (kg/kg)
$\Delta\omega_{g,i}$	deviance from saturation (kg/kg)

Subscripts

acl	anode catalyst layer
agdl	anode gas diffusion layer
ccl	cathode catalyst layer
cgdl	cathode gas diffusion layer
e	entrance
g	gas
i	component i
j	component j
l	liquid
m	membrane
n	neighboring cells
R	due to chemical reaction
T	due to mass transport (evaporation/condensation)

Superscripts

k	previous iteration
$k+1$	next iteration

and electro-osmotic drag. Diffusion can be limited by thickening the polymer electrolyte membrane; however, by doing so, the ohmic resistance of the membrane increases, therefore decreasing the cell's voltage and power. The electro-osmotic drag is caused by hydrogen ions dragging fluid across the membrane. Ren et al. [4] showed that the electro-osmotic drag terms must be used to accurately describe the methanol cross-over.

There have been several fuel cell models, ranging in dimension and physical characteristics they capture. Garcìa et al. [3] developed a semi-analytical, one-dimensional model that included methanol diffusion and electro-osmotic drag effects. They considered the anode gas diffusion and catalyst layer, as well as the membrane. Kulikovsky [5] also examined the anode side of the DMFC to look at the effect of non-Tafel kinetics on cell performance using a

one-dimensional model. Jeng and Chen [6] developed a 1d model to capture the anode side of a DMFC. The fuel was delivered to their fuel cell by a feed stream using a mass transfer coefficient.

Kulikovsky [7] and Kulikovsky et al. [8] presented 2-dimensional fuel cell models that used liquid and gaseous methanol feeds, respectively. These models examined the use of conventional current collectors compared to embedded current collectors. The conventional current collectors are "sandwiched" on either side of the fuel cell, while the embedded current collects are embedded onto the sides of the diffusion and catalyst layers. They found that an embedded type current collector gives a more uniform concentration and current density, while a conventional current collector produces regions of high current densities and low concentrations. They used flow channels to deliver the fuel in their models. Also the convective transport of the methanol was considered, along with the electrical potential equations of the membrane and carbon phases.

All of the aforementioned models used a single phase approach to the DMFC. Wang and Wang [9] modeled the DMFC used a two-phase mixture model (M^2 model), with a drift flux model to describe the two-phase flow and transport in fluid channels. The M^2 model is a reformulation of two-phase flow into a single equation. The liquid saturation of the void space in the porous media was calculated by making the volume averaged density of one component equal to the volume average density of the saturated value of that component. This component is carbon dioxide on the anode side and water on the cathode side. Also, the species in the liquid and gas phases are considered to be in thermodynamic equilibrium.

Polymer electrolyte membrane fuel cells (PEMFCs) have been more extensively studied using two-phase models. Two-phase transport is crucial in PEMFCs because of flooding effects (liquid blockage of oxidant to the catalyst layer), and membrane drying effects (loss of proton conductivity when membrane is not saturated with water). PEMFCs are very similar to the DMFC because they share the same electrolyte. Nam and Kaviani [10] directly solved for the liquid saturation in a one-dimensional model of the diffusion medium and not the fuel cell. They included condensation effects in their model. They suggest a two-layer diffusion media which creates a saturation jump, which ultimately improves cell performance.

Pasaogullari and Wang [11] used the M^2 model to solve two-phase flow. Unlike Wang and Wang [9], Pasaogullari and Wang [11] directly solved a flow equation for the liquid saturation when using the M^2 model. Similar to Nam and Kaviani [10], they found that a two-layer gas diffusion media enhances liquid-water removal from the fuel cell and reduces the liquid-saturation in the catalyst layers.

Natarajan and Nguyen [12] also solved the multiphase flow problem in a PEMFC. The capillary pressure was calculated using an exponential function as opposed to the polynomial Leverett function used in the other multiphase models. Their model captured transient characteristics for the cathode of a fuel cell and included evaporation and condensation effects.

One of the driving characteristics of research on DMFCs is the potential for portable application. In order to utilize all of the power produced, it would be beneficial to operate these fuel cells in the passive mode, with no moving parts such as pumps, fans, and blowers. Faghri and Guo [13,14] developed an innovative passive fuel delivery system that uses a preferential wicking material to separate the fuel storage system from the fuel delivery system. This system uses a porous material to deliver the methanol to the anode at a controlled concentration. Their system can be used in a planar configuration, therefore making the cell power output easily adjustable by the total cell size, Guo and Faghri [15,16].

There is a lack of multiphase models for the DMFC, especially those including the evaporation/condensation effects. To the author's knowledge, there are no other transient, multiphase models that consider non-equilibrium effects in a DMFC. Also, there is a need for models of a passive fuel delivery system. Water and fuel management are crucial issues to the DMFC, and therefore are very important to include in the numerical model. It is the purpose of this paper to create a transient, multi-phase, multi-component model that includes evaporation/condensation effects as well as solving realistic electrochemistry. The non-equilibrium effects of the methanol/water evaporation/condensation are also captured. This model performs two tasks. First, the DMFC is characterized, focusing on optimal operating conditions based on cell power output and fuel consumption efficiency. Second, this paper addresses issues such as water/fuel management, start-up characteristics and limiting the amount methanol cross-over for a passive fuel delivery system.

2. Problem formulation

The current problem is formulated in two parts. First, the fuel cell is characterized as a function of methanol feed concentration. In these simulations a droplet of methanol solution is applied directly to the anode side of the fuel cell, as shown in Fig. 1a. With these simulations, the operating parameters that effect the cell's power output and fuel consumption efficiency are examined. Second, the passive fuel delivery system is examined. The general schematic for the proposed passive fuel delivery system for a DMFC is presented in Fig. 1b. There are several components in this system, the components and their functions are:

- Methanol storage tank, to store liquid methanol;
- Preferential wicking material to prevent back diffusion of water into the storage tank;
- Non-preferential wicking material to deliver the methanol to the fuel cell and control the methanol concentration at the anode side to limit methanol cross-over;
- Fuel cell (anode/cathode diffusion layers, catalyst layers and polymer electrolyte membrane);

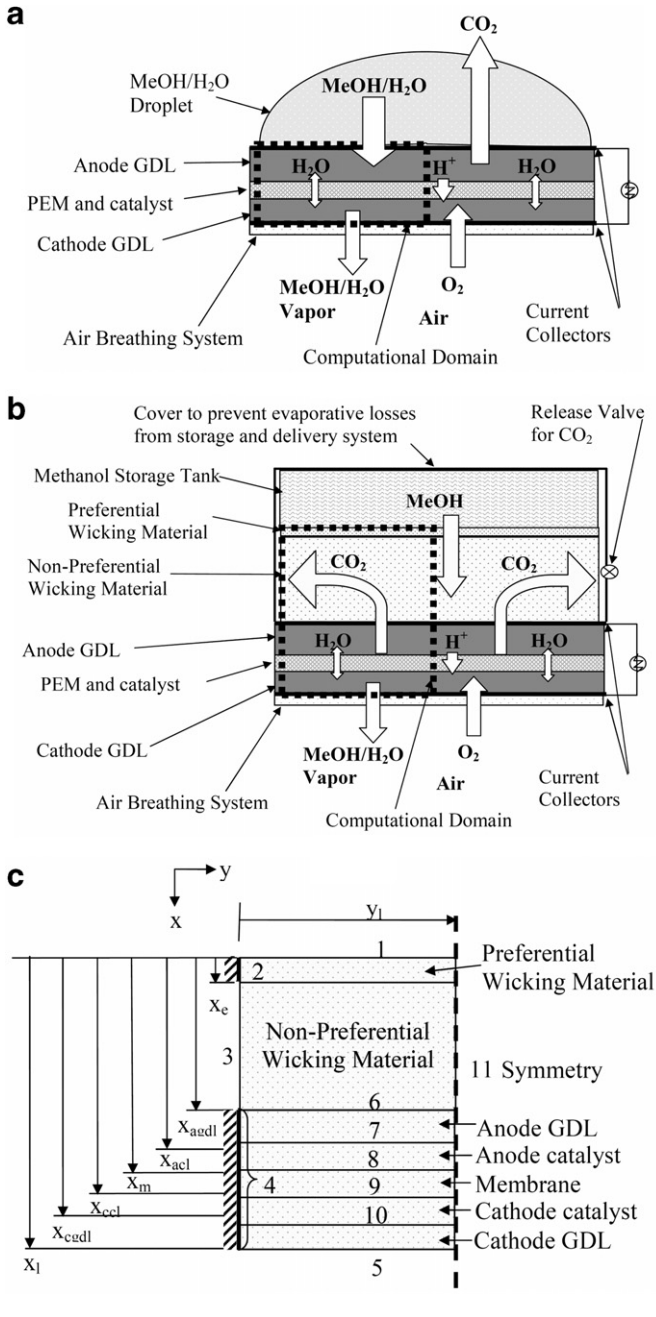

Fig. 1. Schematic of the (a) DMFC with a fuel droplet, (b) the passive fuel delivery system and DMFC, (c) and the computational domain and boundaries.

- Air-breathing System, hydrophobic material to prevent water droplet formation on the cathode side;
- Current Collectors, connected to external circuit to produce power.

The preferential wicking material is hydrophilic to methanol and hydrophobic to water. The contact angles for hydrophilic and hydrophobic materials are

$$\theta_{\text{Hydrophilic}} < \frac{\pi}{2}, \quad \theta_{\text{Hydrophobic}} \geqslant \frac{\pi}{2}.$$

When water diffuses into the preferential wicking material, the capillary pressure tends to reject its entrance. This process rejects the entrance of water into the methanol storage tank. The non-preferential wicking material is hydrophilic to both methanol and water, and is suitable for deliver of liquid methanol to the fuel cell. The thickness of this region helps control the concentration of methanol at the anode side and also the start-up time.

2.1. Flow equations

The continuity equations for the liquid and gaseous phases in a porous zone are given in Eqs. (1a) and (1b), respectively. These equations apply to every region simulated since they are all porous.

$$\frac{\partial}{\partial t}(\varepsilon s \rho_{\text{l}}) + \nabla \cdot (\varepsilon s \rho_{\text{l}} \langle \mathbf{V}_{\text{l}} \rangle^{l}) = \dot{m}_{\text{l}}''' \tag{1a}$$

$$\frac{\partial}{\partial t}(\varepsilon (1-s) \rho_{\text{g}}) + \nabla \cdot (\varepsilon (1-s) \rho_{\text{g}} \langle \mathbf{V}_{\text{g}} \rangle^{g}) = \dot{m}_{\text{g}}''' \tag{1b}$$

The subscript 'l' refers to the liquid phase while 'g' refers to the gaseous phase. The saturation of the liquid phase is defined as

$$s = \frac{\alpha_{\text{l}}}{\varepsilon} = \frac{\int_{V_{\text{l}}} \mathrm{d}V}{\int_{V_{\text{l}}} \mathrm{d}V + \int_{V_{\text{g}}} \mathrm{d}V} \tag{2}$$

The liquid volume fraction in is α_{l} and ε is the porosity. The velocity used is the intrinsic phase averaged velocity.

$$\langle \mathbf{V}_{\text{l}} \rangle^{l} = \frac{1}{V_{\text{l}}} \int_{V_{\text{l}}} \mathbf{V}_{\text{l}} \mathrm{d}V, \quad \langle \mathbf{V}_{\text{g}} \rangle^{g} = \frac{1}{V_{\text{g}}} \int_{V_{\text{g}}} \mathbf{V}_{\text{g}} \mathrm{d}V \tag{3}$$

The pore Reynolds number is defined a function of the intrinsic velocity and the pore characteristic diameter $\left(d_{\text{pore}} = \frac{\mathbf{K}^{1/2}}{\varepsilon^{1/2}}\right)$.

$$Re_{\varepsilon} = \frac{\rho |\langle \mathbf{V}_k \rangle^{k}| \mathbf{K}^{1/2}}{\mu_k \varepsilon^{1/2}} \tag{4}$$

This Reynolds number is much less than unity, where k refers to either the liquid or gas phase, therefore the inertial terms in the momentum equations can be neglected without compromising the accuracy of the solution. The liquid and gaseous momentum equations are based on Darcy's law with an added electro-osmotic drag term.

$$\varepsilon s \langle \mathbf{V}_{\text{l}} \rangle^{l} = -\frac{k_{\text{rl}} \mathbf{K}}{\mu_{\text{l}}} \nabla p_{\text{l}} + \frac{n_d M_{\text{l}}}{\rho_{\text{l}}} \frac{\mathbf{I}_p}{F} \tag{5a}$$

$$\varepsilon (1-s) \langle \mathbf{V}_{\text{g}} \rangle^{g} = -\frac{k_{\text{rg}} \mathbf{K}}{\mu_{\text{g}}} \nabla p_{\text{g}} \tag{5b}$$

The liquid momentum uses the electro-osmotic drag term from Ren et al. [4], caused by the hydrogen atoms passing from the anode catalyst layer to the cathode catalyst layer. The relative permeability for each phase is defined as

$$k_{\text{rl}} = (s + 0.05)^3 \tag{6a}$$

$$k_{\text{rg}} = (1.05 - s)^3 \tag{6b}$$

The shift of 0.05, in the saturation prevents the relative permeability from going to zero. Therefore, numerical difficulties in the limits of fully saturated or unsaturated pores are avoided. It also allows for liquid to enter regions that were once unsaturated. The momentum equations (Eqs. (5a) and (5b)) can be directly inserted to the continuity equations (Eqs. (1a) and (1b)) to get equations to solve for pressure and liquid saturation.

$$\frac{\partial}{\partial t}(\varepsilon s\rho_{\mathrm{l}}) + \nabla\cdot\left(-\rho_{\mathrm{l}}\frac{k_{\mathrm{rl}}\mathbf{K}}{\mu_{\mathrm{l}}}\nabla p_{\mathrm{l}}\right) = \dot{m}'''_{\mathrm{l}} - \nabla\cdot\left(n_d M_{\mathrm{l}}\frac{\mathbf{I}_p}{F}\right) \quad (7a)$$

$$\frac{\partial}{\partial t}(\varepsilon(1-s)\rho_{\mathrm{g}}) + \nabla\cdot\left(-\rho_{\mathrm{g}}\frac{k_{\mathrm{rg}}\mathbf{K}}{\mu_{\mathrm{g}}}\nabla p_{\mathrm{g}}\right) = \dot{m}'''_{\mathrm{g}} \quad (7b)$$

The gaseous and liquid pressures are related by the capillary pressure. The capillary pressure is defined by the Leverette function.

$$p_{\mathrm{g}} - p_{\mathrm{l}} = p_{\mathrm{c}} = \sigma\cos\theta\left(\frac{\varepsilon}{K}\right)^{1/2} J(s) + p_{\mathrm{shift}} \quad (8)$$

where $J(s)$ is

$$J(s) = \begin{cases} 1.417(1-s) - 2.120(1-s)^2 + 1.263(1-s)^3 & \theta < \pi/2.0 \\ 1.417s - 2.120s^2 + 1.263s^3 & \theta \geqslant \pi/2.0 \end{cases} \quad (9)$$

The term p_{shift} in Eq. (8), compensates for the continuous formulation of the liquid and gaseous phase at low and high saturation levels, respectively. The shift in pressure is less than 1% of the maximum capillary pressure. A hydrophobic region at low saturation levels will not be continuous, and therefore the liquid droplets inside the porous zone are "trapped". Since the porous zone retains these droplets, the porous material is modeled as slightly hydrophilic at very low saturation values in the continuous approach. The same is true for the gas phase in a hydrophilic material at high saturation values. The mass source terms in the governing equations are due to chemical reactions, and by mass transport, i.e. evaporation/condensation. Therefore, the mass source terms are separated into two terms.

$$\dot{m}''' = \dot{m}'''_{\mathrm{R}} + \dot{m}'''_{\mathrm{T}} \quad (10)$$

The subscripts, 'R' and 'T' denote the reaction and mass transport terms, respectively. In the liquid phase, there are only two species, water and methanol; therefore a single species transport equation for methanol with Fickian diffusion is utilized. The increased resistance to the diffusion because of the porosity, saturation and tortuosity, τ, is represented by $[\varepsilon s]^{\tau}$.

$$\frac{\partial}{\partial t}(\varepsilon s\rho_{\mathrm{l}}\omega_{\mathrm{l},i}) + \nabla\cdot\left(-\rho_{\mathrm{l}}\omega_{\mathrm{l},i}\frac{k_{\mathrm{rl}}\mathbf{K}}{\mu_{\mathrm{l}}}\nabla p_{\mathrm{l}}\right) = \nabla\cdot\left([\varepsilon s]^{\tau}\rho_{\mathrm{l}}D_{\mathrm{l},12}\nabla\omega_{\mathrm{l},i}\right) + \dot{m}'''_{\mathrm{l},i} - \nabla\cdot\left(n_{d,i}M_{\mathrm{l},i}\frac{\mathbf{I}_p}{F}\right) \quad (11)$$

The advection term (second term on left) already substitutes the pressure–velocity relationship. The drag coefficient of phase i, is

$$n_{d,i} = x_i n_d \quad (12)$$

The mole fraction of the ith component is denoted by x_i. In the gas phase, there are several components, which are O_2, CO_2, H_2O, CH_3OH and N_2. For increased accuracy, a Stefan–Maxwell diffusion model is used. The Stefan–Maxwell equation is

$$\rho_{\mathrm{g}}\nabla\omega_{\mathrm{g},i} = \sum_{j=1}^{N}\frac{M_{\mathrm{g}}}{M_j}\frac{(\omega_{\mathrm{g},i}\mathbf{J}_{\mathrm{g},j} - \omega_{\mathrm{g},j}\mathbf{J}_{\mathrm{g},i})}{D_{ij}} \quad (13)$$

The mass flux of species i is $\mathbf{J}_{\mathrm{g},i}$, and the binary diffusion coefficient between species i and j is D_{ij}. The matrix $\mathbf{B}$ is arrived at by manipulation of the Stefan–Maxwell equation. The effective diffusion coefficient is equal to the inverse the matrix $\mathbf{B}$.

$$[D_{\mathrm{eff},ij}] = \mathbf{B}^{-1} \quad (14a)$$

$$B_{ii} = \frac{\omega_i M_{\mathrm{g}}}{D_{iN}M_N} + \sum_{\substack{k=1\\k\neq i}}^{N}\frac{\omega_k M_{\mathrm{g}}}{D_{ik}M_k} \quad (14b)$$

$$B_{ij} = -\omega_i M_{\mathrm{g}}\left(\frac{1}{D_{ij}M_j} - \frac{1}{D_{iN}M_N}\right), \quad i \neq j \quad (14c)$$

$$\mathbf{J}_{\mathrm{g},i} = -\sum_{j=1}^{N-1}\rho_{\mathrm{g}}D_{\mathrm{eff},ij}\nabla\omega_{\mathrm{g},j} \quad (14d)$$

There are N total species in the gas. The Nth species equation is satisfied by the overall gas continuity equation and does not need to be solved. This specie is designated to N_2 since it does not partake in any of the chemical reactions or mass transport processes between phases. The ith species equation for the gas phase is

$$\frac{\partial}{\partial t}(\varepsilon(1-s)\rho_{\mathrm{g}}\omega_{\mathrm{g},i}) + \nabla\cdot\left(-\rho_{\mathrm{g}}\omega_{\mathrm{g},i}\frac{k_{\mathrm{rg}}\mathbf{K}}{\mu_{\mathrm{g}}}\nabla p_{\mathrm{g}}\right) = \nabla\cdot\left(-[\varepsilon(1-s)]^{\tau}\mathbf{J}_{\mathrm{g},i}\right) + \dot{m}'''_{\mathrm{g},i} \quad (15)$$

The increased resistance to the diffusion of the gas phase due to the porosity, partial saturation and tortuosity is denoted by $\varepsilon(1-s)^{\tau}$, in front of the diffusive flux term. The summation of the components' mass fractions in both the liquid and gas phases is unity.

$$\omega_{\mathrm{l,MeOH}} + \omega_{\mathrm{l},H_2O} = 1 \quad (16a)$$

$$\sum_{i=1}^{N}\omega_{\mathrm{g},i} = 1 \quad (16b)$$

The evaporation/condensation of the methanol and water are assumed to have vapor pressures that are independent of each other. The partial vapor pressures are determined by the Clapeyron–Clausius equation:

$$p_{\mathrm{g},i,\mathrm{sat}} = p_0\exp\left(\frac{h_{\mathrm{lv}}M_i}{R_u}\left(\frac{1}{T_0} - \frac{1}{T}\right)\right) \quad (17)$$

Since the gas phase is assumed to be ideal, the saturation value of the vapor is

$$\omega_{g,i,sat} = \frac{p_{g,i,sat} M_i}{\rho_g R_u T} \tag{18}$$

The evaporation/condensation term is

$$-\dot{m}'''_{T,l,i} = \dot{m}'''_{T,g,i} = a_{sf}\rho_g h_{m,i}\left(\omega_{g,i,sat} - \omega_{g,i}\right)\omega_{l,i} \tag{19}$$

where a_{sp} and $h_{m,i}$ are the specific area and mass transfer coefficient, respectively. The liquid is a binary mixture, and the potential of one component to evaporate is equivalent to that component's mass fraction, which is accounted for by $\omega_{l,i}$. The Sherwood number for evaporation in a pore is considered unity. This assumption is due to the dominance of diffusion within the pores, because they are extremely small in scale. Also, more elegant formulations of this value would offer little improvement to the overall accuracy of the transport between phases because of the lack of knowledge of the networking of void space filled with gas. Therefore the mass transfer coefficient is

$$Sh = \frac{h_{m,i} d_g}{2D_{eff,ii}} = 1, \quad \text{therefore } h_{m,i} = \frac{2D_{eff,ii}}{d_g} \tag{20}$$

The specific surface area is expressed as

$$a_{sf} = \frac{6\varepsilon(1-s)}{d_g} \tag{21}$$

The characteristic length of the gaseous region is given by

$$d_g = \left(\frac{K}{s\varepsilon}\right)^{1/2} \tag{22}$$

The characteristic length increases as the saturation decreases, because there is greater region of void space occupied by gas.

2.2. Electrochemistry

The electrochemistry must also be solved, since it governs the reaction rates. There are two-potential fields considered: the potential of the membrane, ϕ_m, and the potential of the carbon phase, ϕ_c. The potential of the membrane phase governs the transport of the protons through the membrane and catalyst layers, and the potential of the carbon phase governs the transport of the electrons in the catalyst and gas diffusion layers, to an external circuit. The carbon and membrane phase potential equations are

$$\nabla\cdot(\sigma_c\nabla\phi_c) - R_{ox} + R_{red} = 0 \tag{23a}$$

$$\nabla\cdot(\sigma_m\nabla\phi_m) + R_{ox} - R_{red} = 0 \tag{23b}$$

The subscripts 'ox' and 'red' refer to the oxidation and reduction reaction rates. The oxidation reaction is taken from Meyers and Newman (2002) and Garcìa et al. (2004).

$$R_{ox} = a_{ox} I_{0,ref}^{MeOH} \frac{c_{MeOH}}{c_{MeOH} + \lambda \exp\left(\alpha_a \eta_a \frac{F}{R_u T}\right)} \exp\left(\alpha_a \eta_a \frac{F}{R_u T}\right) \tag{24}$$

The specific surface area of the catalyst layers is denoted by a, the exchange current density is $I_{0,ref}^{MeOH}$, and k and λ are constants. The reduction reaction is based on first order Tafel kinetics.

$$R_{red} = a_{red} I_{0,ref}^{O_2} \frac{\omega_{O_2}}{\omega_{O_2,ref}} \exp\left(-\alpha_c \eta_c \frac{F}{R_u T}\right) \tag{25}$$

The anode and cathode over-potentials are denoted by η_a and η_c, respectively.

$$\eta_a = \phi_c - \phi_m - U^{MeOH} \tag{26a}$$

$$\eta_c = \phi_c - \phi_m - U^{O_2} \tag{26b}$$

Since the reaction rates are defined, the mass source terms due to chemical reactions can be specified. The oxidation is assumed to occur in the liquid phase, because the liquid covers the Pt/Ru catalyst. Since oxygen and carbon dioxide are not considered in the liquid phase, consumption and production due to chemical reaction for these components is only considered in the gaseous phase. The water formation due to chemical reaction is assumed to be produced in the liquid phase.

$$\dot{m}'''_{R,l} = -\frac{R_{ox}}{6F}(M_{H_2O} + M_{MeOH}) + \frac{R_{red}}{2F} M_{H_2O} \tag{27a}$$

$$\dot{m}'''_{R,g} = \frac{R_{ox}}{6F} M_{CO_2} - \frac{R_{red}}{4F} M_{O_2} \tag{27b}$$

$$\dot{m}'''_{R,l,MeOH} = -\frac{R_{ox}}{6F} M_{MeOH} \tag{27c}$$

$$\dot{m}'''_{R,g,CO_2} = \frac{R_{ox}}{6F} M_{CO_2} \tag{27d}$$

$$\dot{m}'''_{R,g,O_2} = -\frac{R_{red}}{4F} M_{O_2} \tag{27e}$$

2.3. Fluid properties

The fluid properties for the liquid phase are based on volume weighted averaging. The volume fraction of methanol in water is defined as

$$\alpha_{l,MeOH} = \frac{\omega_{l,MeOH}\rho_{l,H_2O}}{(1-\omega_{l,MeOH})\rho_{l,MeOH} + \omega_{l,MeOH}\rho_{l,H_2O}} \tag{28}$$

The fluid properties that are calculated using the volume weighted average are the fluid density, viscosity, and surface tension. The contact angle between the liquid and the solid phase is also calculated by the volume weighted average. The general form of a volume weighted property is

$$\Phi_{l,eff} = \alpha_{l,MeOH}\Phi_{l,MeOH} + (1-\alpha_{l,MeOH})\Phi_{l,H_2O} \tag{29}$$

The concentrations are calculated based on volume fractions also (for values of mol/cm^3)

$$c_{\mathrm{MeOH}} = \frac{\alpha_{\mathrm{l,MeOH}}\rho_{\mathrm{l,MeOH}}}{10^6 M_{\mathrm{MeOH}}} \tag{30a}$$

$$c_{\mathrm{H}_w\mathrm{O}} = \frac{(1-\alpha_{\mathrm{l,MeOH}})\rho_{\mathrm{l,H_2O}}}{10^6 M_{\mathrm{H_2O}}} \tag{30b}$$

The mole fraction of methanol is

$$x_{\mathrm{MeOH}} = \frac{c_{\mathrm{MeOH}}}{c_{\mathrm{MeOH}} + c_{\mathrm{H_2O}}} \tag{31}$$

The molecular weight of the fluid is based on the molar averaged value.

$$M_{\mathrm{l}} = x_{\mathrm{MeOH}} M_{\mathrm{MeOH}} + (1 - x_{\mathrm{MeOH}}) M_{\mathrm{H_2O}} \tag{32}$$

The gas phase is considered an incompressible ideal gas. Therefore, the gas density is

$$\rho_{\mathrm{g}} = \frac{P_{\mathrm{ref}} M_{\mathrm{g}}}{R_u T} \tag{33a}$$

$$M_{\mathrm{g}} = \left(\sum_{i=1}^{N} \frac{\omega_{\mathrm{g},i}}{M_i} \right)^{-1} \tag{33b}$$

The reference pressure, P_{ref}, is used because the gauge pressure, p_{g}, varies only slightly compared to the reference pressure.

2.4. Boundary conditions

The location of the boundary conditions is displayed in Fig. 1c. Each number corresponds to a boundary condition at that location. A summary of the boundary conditions for the fuel droplet or fuel delivery system cases is given in Table 1. At the wall (boundaries 2 and 4) and symmetry (boundary 11), there is no liquid or fluid flow, and there is no species or electrical flux through these boundaries.

$$\nabla p_{\mathrm{l}} \cdot \mathbf{n} = \nabla p_{\mathrm{g}} \cdot \mathbf{n} = 0 \tag{34a}$$

$$\nabla \omega_{\mathrm{l},i} \cdot \mathbf{n} = \nabla \omega_{\mathrm{g},i} \cdot \mathbf{n} = 0 \tag{34b}$$

$$\nabla \phi_{\mathrm{c}} \cdot \mathbf{n} = \nabla \phi_{\mathrm{m}} \cdot \mathbf{n} = 0 \tag{34c}$$

At the boundary of the methanol storage tank and the fuel delivery system (boundary 1), the methanol concentration is one in the liquid phase, and saturated in the gas phase. The mass flux of water back into the methanol storage tank is assumed to be negligible. The liquid gauge pressure is zero, and there is no bulk movement of the gas phase. Also, there is no gas diffusion.

$$p_{\mathrm{l}} = 0 \tag{35a}$$

$$\nabla p_{\mathrm{g}} \cdot \mathbf{n} = 0 \tag{35b}$$

$$\omega_{\mathrm{l,MeOH}} = 1 \tag{35c}$$

$$\text{For } i \neq \mathrm{MeOH}: \ \nabla \omega_{\mathrm{g},i} \cdot \mathbf{n} = 0;$$

$$\text{For } i = \mathrm{MeOH}: \omega_{\mathrm{g,MeOH}} = \omega_{\mathrm{g,MeOH,sat}} \tag{35d}$$

The air breathing system is assumed to prevent water formation on the cathode side, because it is hydrophobic and has very small pores. However, this layer is very thin, and adds minimal resistance to the diffusion of the gas, and the gas components are therefore modeled as a convective boundary condition. The gas gauge pressure is zero. This boundary is also the location of the cathode side current collector; it is a constant potential, or a function of the overall cell current times and external resistance (see Table 1 for corresponding case). The boundary conditions between the cathode diffusion layer and the air-breathing system (boundary 5) are

$$\nabla p_{\mathrm{l}} \cdot \mathbf{n} = 0 \tag{36a}$$

$$p_{\mathrm{g}} = 0 \tag{36b}$$

$$\nabla \omega_{\mathrm{l},i} \cdot \mathbf{n} = 0 \tag{36c}$$

$$D_{\mathrm{eff},ii} \nabla \omega_{\mathrm{g},i} \cdot \mathbf{n} = h_{\mathrm{m},i} (\omega_{\mathrm{g},i,\infty} - \omega_{\mathrm{g},i}) \tag{36d}$$

$$\text{Fixed potential}: \phi_{\mathrm{c}} = V_{\mathrm{cell}}, \tag{36e}$$

$$\text{External resistance}: \phi_{\mathrm{c}} = \int_{y=0}^{y=y_{\mathrm{l}}} \sigma_{\mathrm{c}} \nabla \phi_{\mathrm{c}} \cdot \mathbf{n} \, \mathrm{d}A \times R_{\Omega} \tag{36f}$$

On the side of the fuel delivery system (boundary 3), the gas produced from the chemical reaction are allowed to leave the system. The delivery system is enclosed to reduce the loss of water and methanol in the fuel due to evaporation. Liquid droplets do not develop on this surface. The boundary conditions on the edge of non-preferential wicking fuel delivery system are

$$\nabla p_{\mathrm{l}} \cdot \mathbf{n} = 0 \tag{37a}$$

$$\text{If } p_{\mathrm{g}} \geqslant 0 : p_{\mathrm{g}} = 0 \text{ else } \nabla p_{\mathrm{g}} \cdot \mathbf{n} = 0 \tag{37b}$$

$$\nabla \omega_{\mathrm{l},i} \cdot \mathbf{n} = 0 \tag{37c}$$

$$\dot{m}'_{\mathrm{g},i} = -\rho_{\mathrm{g}} \omega_{\mathrm{g},i} \frac{k_{\mathrm{rg}} \mathbf{K}}{\mu_{\mathrm{g}}} \nabla p_{\mathrm{g}} \cdot \mathbf{n} \tag{37d}$$

The boundary conditions for the flow equations for the fuel delivery system are fully specified, and the rest of the boundary conditions are imposed on the electro-chemistry. The potential of the carbon phase at the current collector on the anode side (boundary 6) is constant throughout all the simulations.

Table 1
Boundaries conditions applied to cases using a fuel droplet or a fuel delivery system

	Boundary number										
	1	2	3	4	5	6	7	8	9	10	11
Fuel droplet	N/A	N/A	N/A	34a–c	36a–d	38, 43a–c	39b	39a	39a	39b	34a–c
Fuel delivery	35a–d	34a–c	37a–d	34a–c	36a–d,f	38	39b	39a	39a	39b	34a–c

$$\phi_c = 0 \tag{38}$$

There is no electron flux in the carbon phase at the edge of the anode catalyst layer (boundary 8) or the cathode catalyst layer (boundary 9). Also, there is no proton flux at the edges of the membrane phase (boundaries 7 and 10). These boundary conditions are

$$\nabla\phi_c \cdot \mathbf{n} = 0 \tag{39a}$$

$$\nabla\phi_m \cdot \mathbf{n} = 0 \tag{39b}$$

For the transient solutions, the initial conditions are that the liquid and gas flow fields are zero, therefore their pressures are both constant. The liquid mass fraction of methanol is 1 in the preferential wicking section, and zero every where else. Also, the gas mass fraction is equal to the mass fraction in air.

$$p_l = p_g = 0 \tag{40a}$$

$$x < x_e : \omega_{l,MeOH} = 1, \quad x \geqslant x_e : \omega_{l,MeOH} = 0 \tag{40b}$$

$$\omega_{g,i} = \omega_{g,i,\infty} \tag{40c}$$

To create polarization curves, a separate set of cases were run, in which the methanol solution was directly placed onto the anode gas diffusion layers. For these cases, the fuel delivery system is not modeled and the only different boundary conditions are at boundary 6.

$$p_l = p_g = 0 \tag{41a}$$

$$\omega_{l,MeOH} = \omega_{l,solution} \tag{41b}$$

$$\nabla\omega_{g,i} \cdot \mathbf{n} = 0 \text{ for } i = O_2, CO_2;$$

$$\omega_{g,i} = \omega_{g,i,sat} \text{ for } i = H_2O, MeOH \tag{41c}$$

2.5. Numerical procedure

The equations laid out above are solved numerically using a finite volume scheme. The Gauss-Siedel iteration procedure was used to solve all the flow equations. The liquid flow equation was solved in two steps. First, the liquid saturation was calculated by linearizing liquid flow equation with respect to liquid saturation:

$$a_{c,s}s^{k+1} + a_{c,p}\left(p_g - p_c + \frac{\partial p_c}{\partial s}(s^{k+1} - s^k)\right) + \sum_n a_n p_l = b \tag{42}$$

where the coefficients in the solution matrix are denoted by a, and the answer to the solution matrix is denoted by b. Second, the liquid pressure was directly calculated using the new saturation level calculated in Eq. (45). This process increases the rate of convergence and also allows for real solutions when a pore is fully saturated with liquid.

For the methanol and water vapor mass fraction, the departure from saturation ($\Delta\omega_{g,i}$) was calculated instead of the liquid mass fraction.

$$\Delta\omega_{g,i} = \omega_{g,i} - \omega_{g,i,sat} \tag{43a}$$

$$a_c(\omega_{g,i,sat} + \Delta\omega_{g,i}) + \sum_n a_n(\omega_{g,i}) = b - a_{sf}h_m\omega_{l,i}\Delta\omega_{g,i} \tag{43b}$$

The solution procedure is

1. Solve liquid saturation (Eqs. (7a) and (8) by Eq. (45)).
2. Solve liquid pressure, based on new saturation solved in step 1 (Eq. (7a)).
3. Solve gas pressure (Eq. (7b)).
4. Solve species equations in both liquid and gas (Eqs. (11) and (15)).
5. Solve electric potential equations (Eqs. (23a) and (23b)).
6. Update flow properties.
7. Go to 1 and repeat until converged.

It was found that the residual was not a good convergence criteria since once the residual dropped and flattened out, the solution could change by as much as 15%. Therefore, randomly selected cell values were tracked, and when these cell values changed by less than 0.01% over 50 iterations (percent difference taken from change from previous time step value), the solution was considered converged. The solution typically took 15,000 to 20,000 iterations per time step to converge, when the entire system was modeled.

3. Results

The results are broken into two-sections. The first section characterizes the fuel cell performance, and the results coincide with the fuel applied as a liquid droplet on the anode side, as shown in Fig. 1a. The second section characterizes the start-up characteristics of the passive fuel delivery system shown in Fig. 1b. The physicochemical properties used in the current simulations are presented in Table 2.

3.1. Fuel cell characterization

The fuel droplet applied to the anode side of the fuel cell is a one-dimensional problem because the boundary conditions in the y-direction are all zero-gradient conditions. Therefore, the computational grid has only on cell in the y-direction. In the x-direction there are 50, 20, 30, 20 and 50 cells across the 'agdl', 'acl', 'membrane', 'ccl' and 'cgdl', respectively. To check for grid independence, the grid resolution was reduced by a factor of 2 in all of the zones in the x-direction. The 2M feed concentration case was repeated and the difference in the current density for each cell voltage was less than 1% with the finer mesh.

The chemical reactions of the current simulations are calibrated with the experimental data of Guo and Faghri [15]. The polarization curve comparing the present simulations to the experimental data is shown in Fig. 2. The differences in the data may arise because of the isothermal assumption. The numerical plot is lower at higher current densities. At the higher current densities, the reaction rate is faster, and therefore more heat is produced from the chemical reaction, which increases the cell temperature. Consequently the electro-activity of the methanol

Table 2
Physicochemical properties

Parameter	Value			Ref.
	$K/\varepsilon/\tau$ (m^2/unitless/unitless)	θ, H_2O/MeOH (radians)	p_{shift} (Pa)	
Pref. wick.	2.5e−13/0.8/1	$\pi/0$	$(\theta < \pi/2)$ −100, $(\theta > \pi/2)$ 50	Assumed
Non. pref.	1e−10/0.8/1	0/0	−200	Assumed
agdl	1e−11/0.7/1	0/0	−200	Assumed
acl	2.5e−12/0.6/1.8	0/0	−200	Assumed
mem.	1e−13/0.5/1.8	0/0	0	Assumed
ccl	2.5e−11/0.6/1.8	$\frac{\pi}{3}/0$	−200	Assumed
cgdl	1e−10/0.7/1	π/π	50	Assumed
Diffusivity, gas phase, $D_{ij} = D_{ji}$ (m^2/s)	O_2/CO_2 O_2/H_2O O_2/N_2 CO_2/H_2O CO_2/N_2 H_2O/N_2	0.159×10^{-4} 0.244×10^{-4} 0.162×10^{-4} 0.160×10^{-4} 0.242×10^{-4} at 293 K, 101.325 kPa		Lide [17] for proportionality of form $D_{ij} \propto p^{-1}T^{3/2}$
	O_2/MeOH CO_2/MeOH H_2O/MeOH MeOH/N_2 Assumed	$\begin{pmatrix} -0.06954 \\ +4.5986 \times 10^{-4}T \\ +9.4979 \times 10^{-7}T^2 \end{pmatrix} \times 10^{-4}$		Yaws [18]
Diffusivity, liquid phase (m^2/s)	MeOH/H_2O	$10^{(-5.4163-999.778/T)}$		Yaws [19]
Viscosity, μ (N s/m^2)	Gas phase H_2O	0.1846×10^{-4} 8.55×10^{-4}		Incropera and Dewitt [20]
	MeOH	5.390×10^{-4}		Yaws [19]
Density, $\rho_{l,i}$ (kg/m^3)	H_2O	$\exp\begin{pmatrix} 6.9094 - 2.0146 \times 10^{-5}(T-273) \\ -5.9868 \times 10^{-6}(T-273)^2 + 2.5921 \times 10^{-8}(T-273)^3 \\ -9.3244 \times 10^{-11}(T-273)^4 + 1.2103 \times 10^{-13}(T-273)^5 \end{pmatrix}$		Faghri [21]
	MeOH	$244.4 \times 0.224^{(-(1-\frac{T}{513})^{\frac{2}{7}})}$		Yaws [19]
Electro-osmotic drag coefficient (mol/mol)	n_d	2.5		Ren et al. [4]
Electric conductivity (Ω^{-1} m^{-1})	σ_c σ_m	4000 3.4		Kulikovsky et al. [8]
Transfer coefficient	α_a α_c	0.52 1.55		García et al. [3]
Specific area (m^{-1})	a_{ox} a_{red}	16.09 $\frac{1}{x_{ccl}-x_m} = 43,478$		Fit to data
Exchange current density (A/m^2)	$I_{0,ref}^{MeOH}$ $I_{0,ref}^{O_2}$	$94.25\exp(35{,}570/R(1/353 - 1/T))$ $0.04222\exp(732{,}000/R(1/353 - 1/T))$		Wang and Wang [9]

Oxidation constant (mol/cm^3)	λ	2.4×10^{-9}	Fit to data
Reduction reference mass fraction (kg/kg)	$m_{O_2,\mathrm{ref}}$	0.23	Wang and Wang [9]
Thermodynamic potential (V)	U^{MeOH}	−0.0229	Meyers and Newman [2]
	U^{O_2}	1.24	Wang and Wang [9]
Distance (m)	x_e	2×10^{-4}	
	$x_{agdl} - x_l$	3×10^{-3}	
	$x_{acl} - x_{agdl}$	1.5×10^{-4}	
	$x_m - x_{acl}$	2.3×10^{-5}	
	$x_{ccl} - x_m$	1.8×10^{-4}	
	$x_{cgdl} - x_{ccl}$	2.3×10^{-5}	
	$x_l - x_{cgdl}$	1.5×10^{-4}	
	y_l	5×10^{-3}	

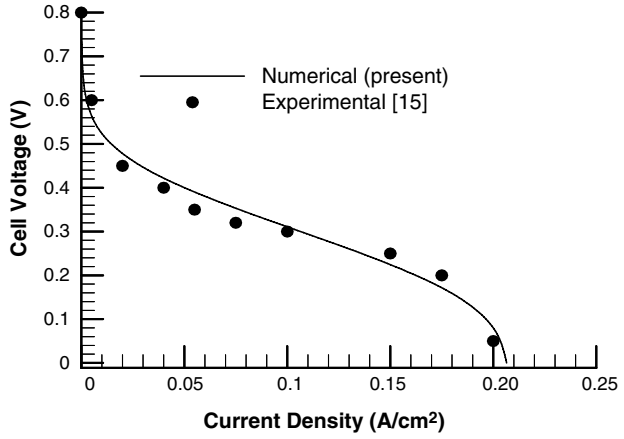

Fig. 2. Comparison of numerical and experimental polarization curves, for 2 M methanol feed concentration at 300 K.

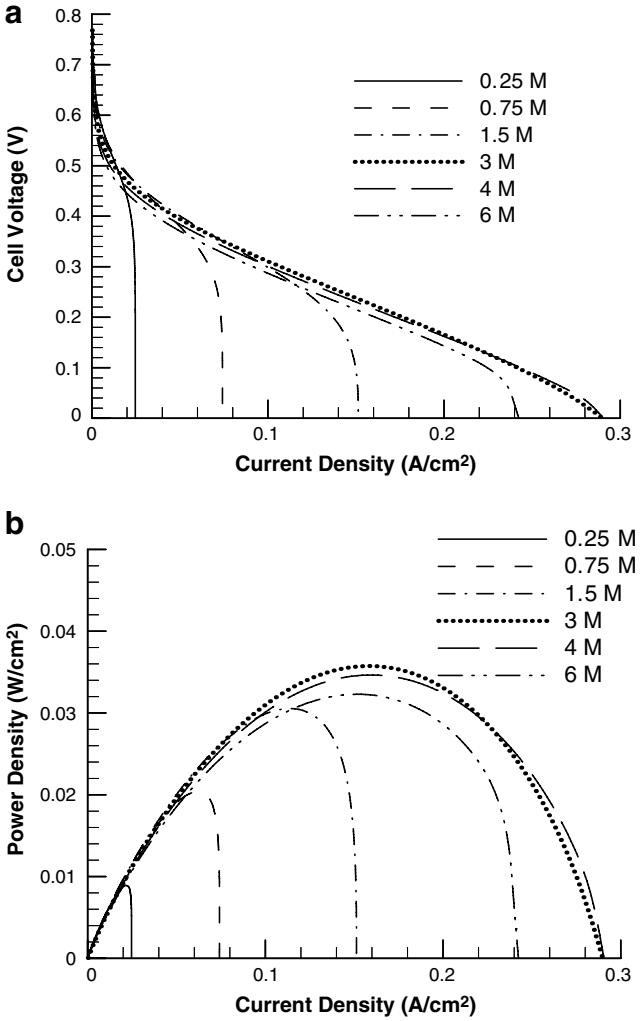

Fig. 3. The effect of methanol concentration on the (a) polarization curve (b) and the corresponding cell power density at a cell temperature of 300 K.

oxidation is increased. Characterizing the thermal transport in the fuel cell is the subject of ongoing research.

The effect of methanol feed concentration on the polarization curves is presented in Fig. 3a. Each polarization curve has the same general trend: an initial drop in cell voltage with the current density remaining small; a near linear region where the methanol oxidation is reaction rate limited; finally a steep drop in cell voltage while the cell current density remains constant, corresponding to the mass transfer limited region. At the higher methanol concentrations, the reaction rate is not mass transfer limited; however if the concentration is too high, the methanol crossover will dominate and lead to lower cell currents. The corresponding power densities are presented in Fig. 3b. The maximum power density is located at a slightly lower current density than the mass limited region. The maximum power generally increases with methanol feed concentration, until the methanol cross-over effects become significant. Once the cross-over is too great, the cell performance begins deteriorating.

The maximum cell power vs. methanol feed concentration is plotted in Fig. 4a. The cell power density increases until the methanol feed concentration is about 3 M, then the cell power begins to decay. To understand the decay, the fuel consumption efficiency is plotted in the same figure.

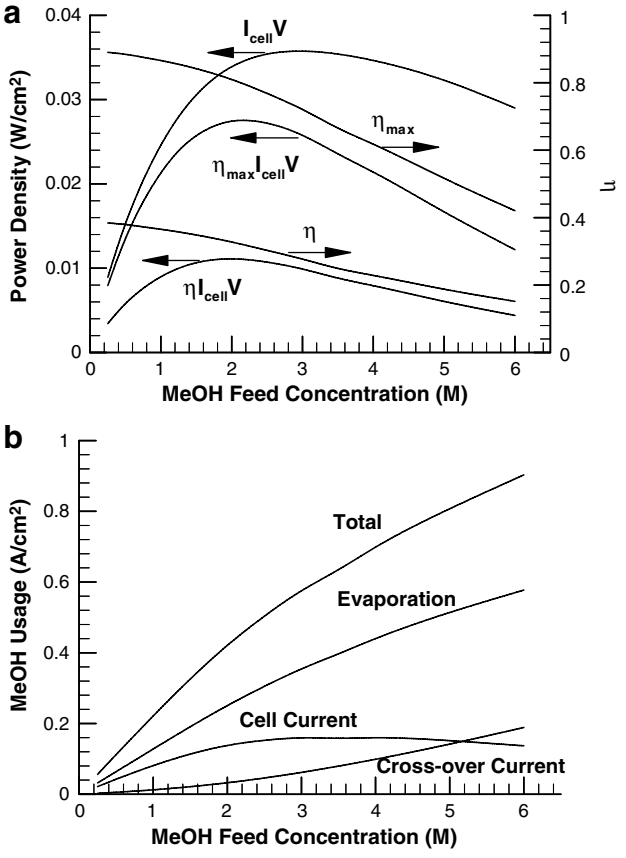

Fig. 4. (a) Maximum power density and associated fuel consumption efficiency vs. methanol feed concentration and (b) total methanol usage at maximum power vs. feed concentration at cell temperature of 300 K.

$$\eta = \frac{\mathbf{I}_{\text{cell}}}{\mathbf{I}_{\text{cell}} + \mathbf{I}_{\text{cross-over}} - \frac{6F}{M_{\text{MeOH}} A} \int \dot{m}'''_{\text{T,l,MeOH}} \mathrm{d}V} \tag{44}$$

The fuel consumption efficiency measures the amount of fuel used to create power, compared to the total amount of fuel used. The most efficient fuel usage is at the lowest concentrations, and decreases as the methanol feed concentration increases. When multiplying the consumption efficiency by the maximum cell power, the concentration at which the maximum cell power is achieved shifts slightly to a lower concentration (from approximately 3 M to approximately 2 M). Since most of the fuel loss is due to evaporation, it has potential to be recovered. Assuming there is a process to recover all of the vapor, the maximum fuel consumption efficiency, $\eta_{\max}$, is defined.

$$\eta_{\max} = \frac{\mathbf{I}_{\text{cell}}}{\mathbf{I}_{\text{cell}} + \mathbf{I}_{\text{cross-over}}} \tag{45}$$

Designing a fuel recovery system has the potential to increase the fuel consumption efficiency by close to 250% near the maximum power density.

The three factors in fuel consumption are the fuel used to produce useful current (cell current), the fuel wasted by reacting at the cathode catalyst layer (cross-over current) and the fuel evaporated. The overall fuel consumption at the maximum power density is plotted in Fig. 4b. The fuel used by evaporation is always increasing over the feed concentrations considered. The cell current increases with methanol feed concentration, until the concentration reaches 3 M. At this point the cell current density begins to decrease because the cross-over current is increasing. At approximately 5.3 M feed concentration, the cross-over current becomes greater than the cell current.

The transport of the methanol through the membrane is caused by diffusion, electro-osmotic drag and by pressure. These effects were calculated at the entrance beginning of the membrane ($x = x_{\text{m}}$).

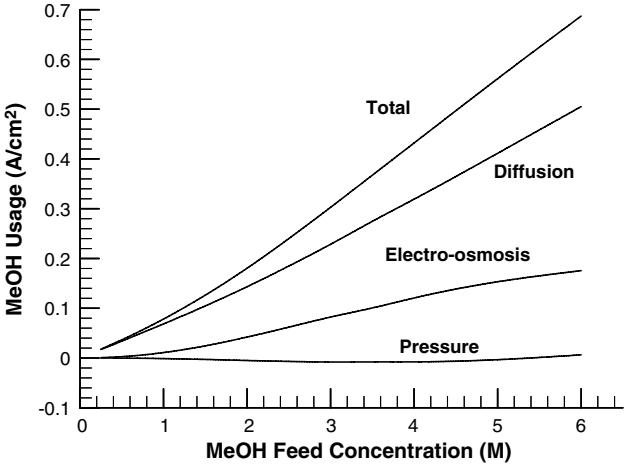

Fig. 5. Methanol crossover vs. methanol feed concentration at maximum power density at cell temperature of 300 K.

$$\mathbf{I}_{\text{diffusion}} = \frac{6F}{M_{\text{MeOH}}A}\int_{x=x_{\text{m}}}(-\rho_{\text{l}}(\varepsilon s)^{\tau}D_{\text{l},12}\nabla\omega_{\text{l,MeOH}})\mathrm{d}A \quad (46a)$$

$$\mathbf{I}_{\text{electro-osmosis}} = \frac{6}{M_{\text{MeOH}}A}\int_{x=x_{\text{m}}}(n_{d,\text{MeOH}}M_{\text{MeOH}}\mathbf{I}_{p})\mathrm{d}A \quad (46b)$$

$$\mathbf{I}_{\text{pressure}} = \frac{6F}{M_{\text{MeOH}}A}\int_{x=x_{\text{m}}}\left(-\rho_{\text{l}}\omega_{\text{l,MeOH}}\frac{k_{\text{rl}}\mathbf{K}}{\mu_{\text{l}}}\nabla p_{\text{l}}\right)\mathrm{d}A \quad (46c)$$

$$\mathbf{I}_{\text{tot,cross-over}} = \mathbf{I}_{\text{diffusion}} + \mathbf{I}_{\text{electro-osmosis}} + \mathbf{I}_{\text{pressure}} \quad (46d)$$

These transport processes driving the methanol cross-over are presented in Fig. 5, along with the total methanol cross-over. Diffusive transport is the dominant reason that methanol crosses over the polymer electrolyte membrane. The diffusion grows nearly linearly with increased methanol feed concentration. This linear growth is because the methanol concentration stays very small at the cathode catalyst layer due to evaporation and methanol oxidation, therefore increasing the methanol concentration gradient through the membrane. The electro-osmotic effect increases with increasing methanol concentration; the increase is due to the increased methanol concentration and cell current at the lower feed concentrations. As the feed concentration increases past 3 M, the cell current begins to reduce, however the electro-osmosis continues to increase. The increase is because this drag is an advection process and the feed concentration is increasing. The rate of change of electro-osmosis becomes negative when the feed concentration is greater than 3 M because of the reduced current density. Finally, the pressure tends to drive the liquid back through the membrane because the rate at liquid (water) is produced at the cathode catalyst layer due to the reduction reaction is greater than the rate at which liquid (water and methanol) is evaporated. As the methanol concentration increases, the evaporation rate increases because methanol is more volatile than water, and at approximately 5.4 M methanol feed concentration, the evaporation rate is greater than the water production rate by chemical reaction.

In order to design an effective fuel cell system, the optimal range of operation must be known. The contour plots of cell power density and the cell power density times the

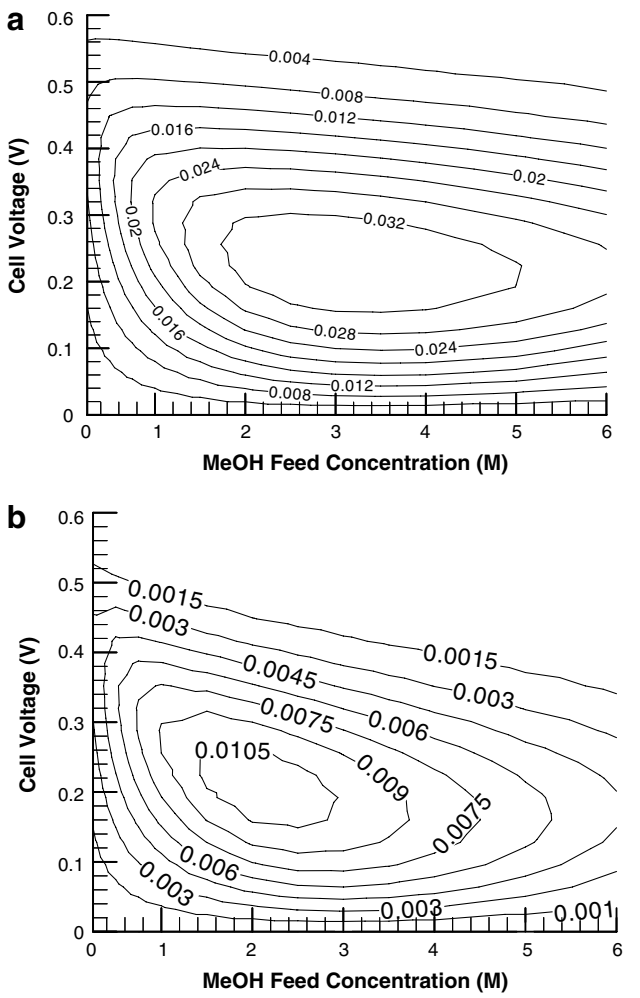

Fig. 6. Contour plots of (a) cell power density (W/cm^2), and (b) cell power density * η (W/cm^2) as a function of MeOH feed concentration and cell voltage at cell temperature of 300 K.

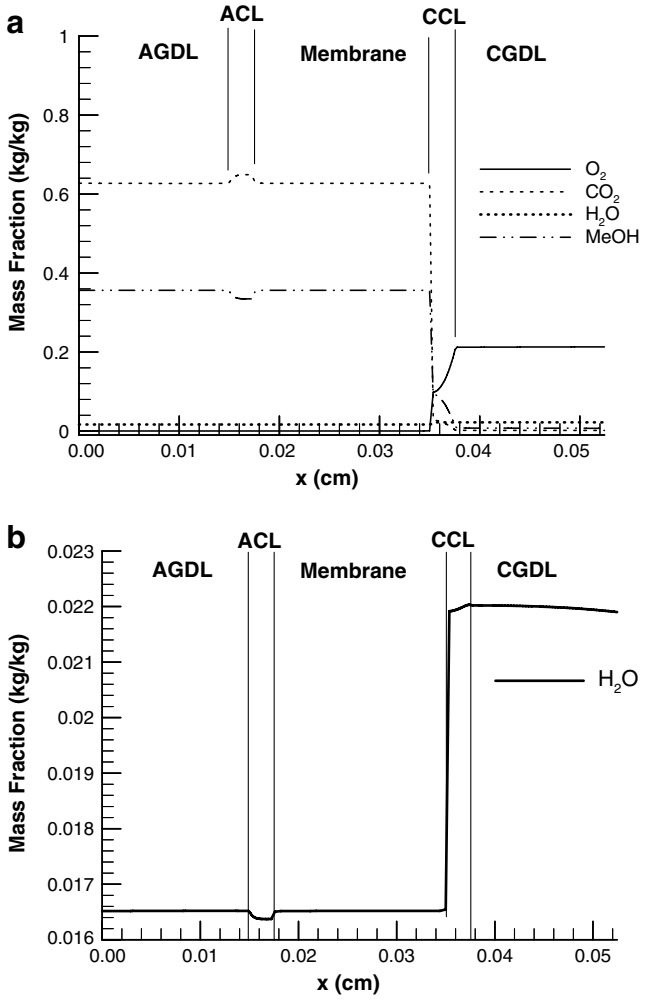

Fig. 7. Area averaged gas phase species mass fraction vs. distance through the fuel cell at 2.02 M, 0.245 V at cell temperature of 300 K (a) for all species and (b) for water vapor.

fuel consumption efficiency vs. methanol feed concentration and cell voltage are presented in Figs. 6a and b, respectively. The optimal operating conditions of a DMFC lie in the inner circle of both contour plots (inside 0.032 W/cm^2 in 6a, and inside 0.0105 W/cm^2 in 5b). By considering the methanol cross-over effects, the methanol feed concentration should be between approximately 1.5 M and 2.5 M, with a cell voltage between 0.2 and 0.25 V. This operating range is much tighter than the range when only considering maximum power output, 2 M to 4.5 M with a cell voltage between 0.2 and 0.3 V. The optimal methanol feed concentration and cell voltage were found to be 2.02 M and 0.245 V, based on the product of the maximum power output and fuel consumption efficiency plotted in Fig. 4a. These values fall within the optimal operating ranges based on power output with and without the fuel consumption efficiency.

The transport of the gas phase is important because of the oxygen needed in the reduction reaction, the carbon dioxide generated in the oxidation reaction and the evaporation rate depends on the mass fraction of water and methanol vapor, compared to their respective saturation values. The area averaged mass fraction of these components is presented in Fig. 7a. Due to scale, the water vapor mass fraction is presented in Fig. 7b. The area averaged value is calculated by

$$\overline{\omega_{g,i}} = A^{-1} \int_x \omega_{g,i} \mathrm{d}A \tag{47}$$

The mass fraction of carbon dioxide increases in the 'acl' because of its generation in the oxidation reaction. The methanol and water vapor are transported out of the 'acl' through advection, and consequently have a lower mass fraction in the 'acl'. The lower mass fraction increases the absolute deviance, $|\Delta\omega_{g,i}|$, from saturation, and therefore the evaporation rate increases. The membrane is almost completely saturated ($s > 0.999$), therefore any gas transport is negligible through this region. At the 'ccl' the oxygen is consumed because of the reduction reaction, and carbon dioxide is generated because of the oxidation reaction (cross-over current). Methanol vapor diffuses out of the 'ccl' and into the 'cgdl'. The mass fractions of all the components in the cathode gas diffusion layer (cgdl) are nearly constant because the layer is very thin, and the pores are nearly unsaturated with liquid; therefore the diffusive transport is driven by very small changes in mass fraction. The water vapor mass fraction decreases slightly at the outer edge of the 'cgdl', near the air-breathing system, because the convective transport with the environment interacts with this boundary.

The concentration of methanol in the liquid phase as well as the evaporation rates of methanol and water are presented in Fig. 8. The methanol concentration has a nearly linear slope in the 'agdl' and membrane because the diffusion transport is dominant. Methanol is consumed in the 'acl' and 'ccl' because of chemical reaction and evaporation. The methanol concentration drops sharply after

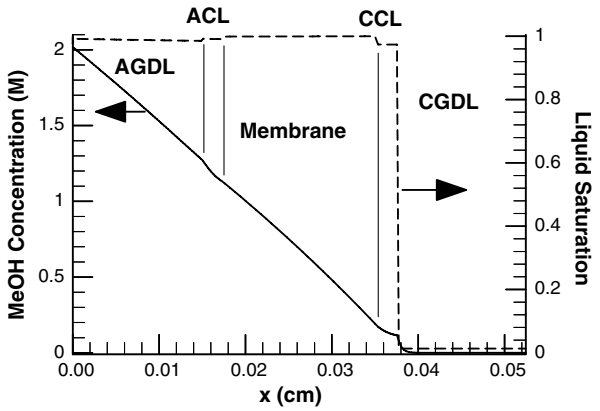

Fig. 8. Area averaged MeOH concentration and liquid saturation vs. distance through the fuel cell at 2.02 M, 0.245 V at cell temperature of 300 K.

the 'ccl', because the methanol evaporates out of solution, and the liquid saturation level is low. The liquid is very nearly saturated in the 'agdl', 'acl', 'membrane' and 'ccl' because they are hydrophilic. The membrane is essentially completely saturated ($s > 0.999$), therefore the gas transport in this region is negligible.

The mass transport of the gases is very dependent on the chemical reactions and the evaporation rates. The production of carbon dioxide and consumption of oxygen by the oxidation and reduction reactions, respectively, are plotted in Fig. 9. The evaporation rates of methanol and water are also plotted in this figure. In the 'acl', evaporation of methanol and water spikes because the gas phase is not saturated with their vapors. The methanol evaporation rate is much higher than the evaporation rate of water because it has a higher partial pressure. In the 'ccl', the reduction reaction is the greatest where the oxygen mass fraction is

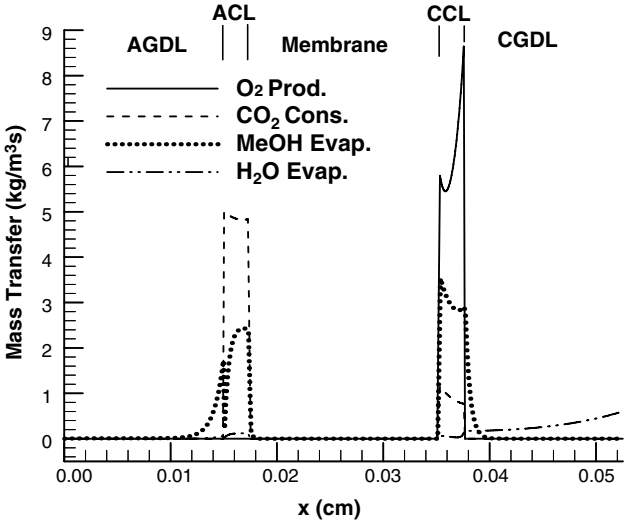

Fig. 9. Area averaged mass transfer effects of chemical reaction and evaporation vs. distance through the fuel cell at 2.02 M, 0.245 V and a cell temperature of 300 K.

the highest. The reduction reaction increases again near the membrane in the 'ccl', because the cathode over-potential decreases in this region. The methanol evaporation rate increases in the 'ccl' because the methanol is directly diffuses to the environment from this region. The methanol is depleted, and goes to zero in the 'cgdl', and thus the evaporation rate goes to zero in this region. The water evaporation rate increases throughout the 'cgdl', because it is exposed to the environment. The evaporation rate of water is the greatest near the edge of the 'cgdl' close to the air-breathing system, because the water vapor diffuses into the environment.

3.2. Start-up characteristics

The fuel cell polarization and transport phenomena have been closely examined. Now the start-up characteristics of the proposed passive fuel delivery system investigated. The active cell area was considered to be 1 cm^2, and the resistance of the external circuit was 1 ohm, for all of the transient cases. The computational mesh had 8, 30, 15, 10, 15, 10 and 15 cells in the x-direction for the preferential wicking, non-preferential, 'agdl', 'acl', 'membrane', 'ccl' and 'cgdl' sections, respectively. The mesh was composed of 20 cells in the y-direction. The time-step size was 30 s. To check for grid independence, a grid of 10, 40, 20, 15, 20, 15 and 20 cells in the x-direction, for the respective sections listed above, and 30 cells in the y-direction was used. The current-density varied by a maximum of 4% (normalized by the max. current density) over the entire simulation.

The start-up cell current density, cell power density and methanol feed concentration (methanol concentration at $x = x_{agdl}$) are presented in Fig. 10. It takes the fuel cell about 20 min to reach a maximum current density and cell power. At this time, the feed concentration is 3 M, which corresponds to the molarity of the maximum power output presented in Fig. 4a. After 20 min, the current density begins to decay because the methanol feed concentration increases, and the cross-over effects begin to degrade the cell's performance. The methanol feed concentration reaches a maximum, while the cell current and power densities reach a relative minimum at approximately 60 min. At this point, the methanol feed concentration decreases slowly, and the cell current and power densities begin to slowly increase.

The fuel consumption of the fuel-cell start up is examined in Fig. 11a. At times earlier than 20 min, the two dominant factors in fuel consumption are the cell current and evaporation. At times greater than 20 min, the evaporation is the major form of fuel consumption. At this time the cross-over current becomes significant, and therefore the cell current reduces. The cross-over current becomes greater than the cell current after 40 min. The methanol transport through the membrane is caused by diffusion, electro-osmosis and pressure as laid out in equations (46a) through (46d). The contribution of each of these

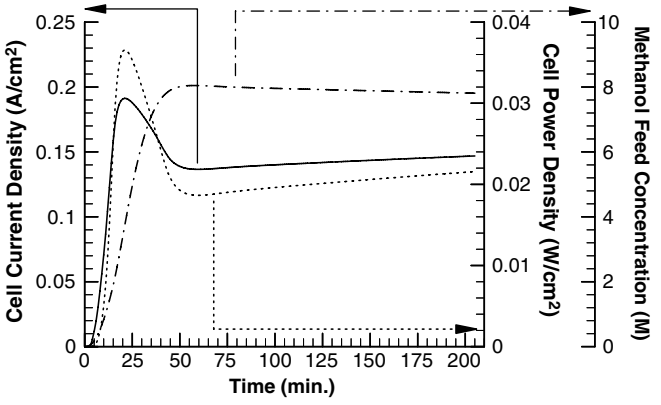

Fig. 10. Start-up current density, cell power and methanol feed concentration vs. time for a non-preferential wicking length of 3 mm, cell area of 1 cm^2 and $R_\Omega = 1\ \Omega$ at cell temperature of 300 K.

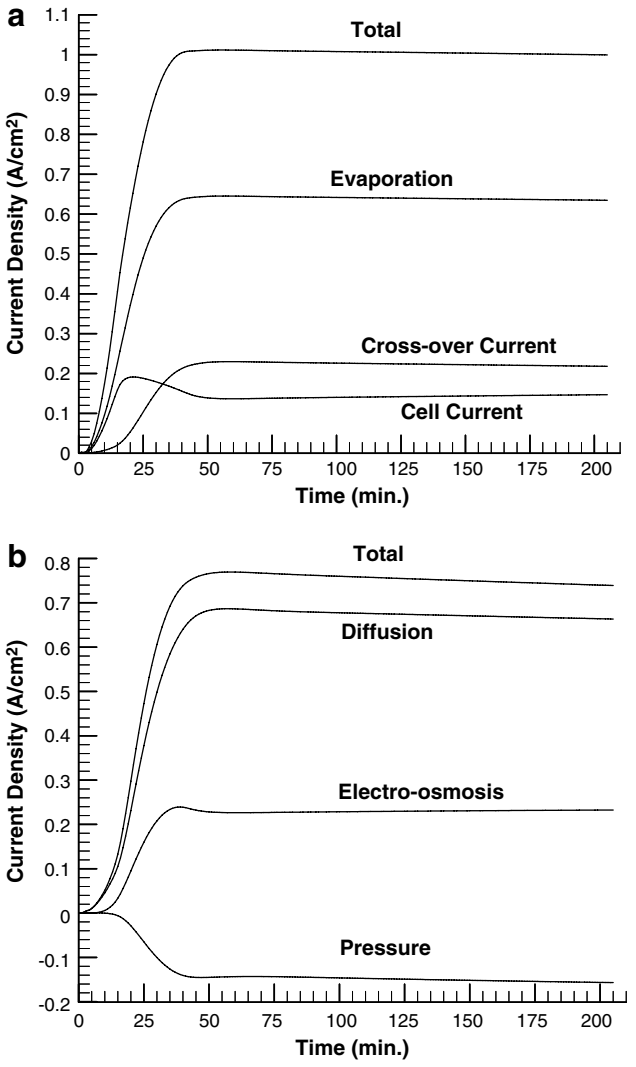

Fig. 11. (a) Fuel usage and (b) methanol cross-over during startup for a passive fuel deliver system with a non-preferential wicking length of 3 mm, cell area of 1 cm^2 and $R_\Omega = 1\ \Omega$ at cell temperature of 300 K.

effects is displayed in Fig. 11b. The diffusion is the greatest contributor to the total cross-over rate of methanol, while electro-osmosis contributes about one third of the transport as diffusion. The pressure drives the flow back through the membrane to the anode, but at a slower rate than the electro-osmosis.

The methanol concentration through the fuel cell and passive delivery system at different times is presented in Fig. 12. The transport of methanol through the delivery system is caused by diffusion and advection. The diffusive transport is more prominent; however the advection process still has an effect. The advection transport of methanol is caused by the liquid flow driven by capillary forces, to make up for the liquid evaporated in the fuel cell. The effect of the advection can be seen on the bowed concentration through the system at times greater than 30 min.

The area averaged liquid mass flux (water and methanol combined) through the delivery system and fuel cell is presented in Figs. 13a and b. The early times are displayed in the former, and the greater times are displayed in the latter. For the first 10 min, the liquid flux is negative near the fuel storage system. This means that water is transported back into the storage tank. However, this value is small; based on 0.1 g/m^2 s, assuming all water fluxed into the storage tank for 10 min, the total mass is 6 mg/cm^2. The assumption of negligible transport of water into the storage tank is valid. As time increases the total liquid flux becomes positive. The liquid water flux reaches a peak at approximately 20 min near the 'acl', which corresponds to the maximum current density. Since the liquid is used up the most rapidly at this time, the net transport in the rest of the delivery system has to increase to make up for the liquid consumed. After 30 min, the water transport through the system begins to slowly decrease, unit it approaches an equilibrium state. Throughout the simulation, the mass flux of liquid sharply decreases in the 'acl' because liquid is evaporated and consumed by the anodic reaction. In the 'ccl' the liquid mass flux drops sharply again to approx-

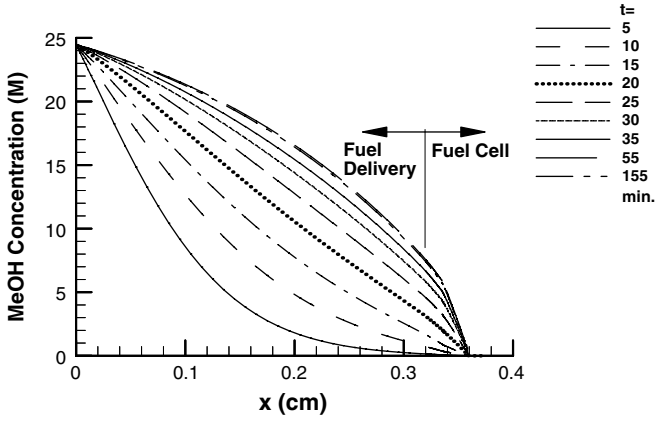

Fig. 12. Methanol concentration vs. distance through the fuel delivery system and fuel cell at different times with a non-preferential wicking length of 3 mm, cell area of 1 cm^2 and $R_\Omega = 1\ \Omega$ at cell temperature of 300 K.

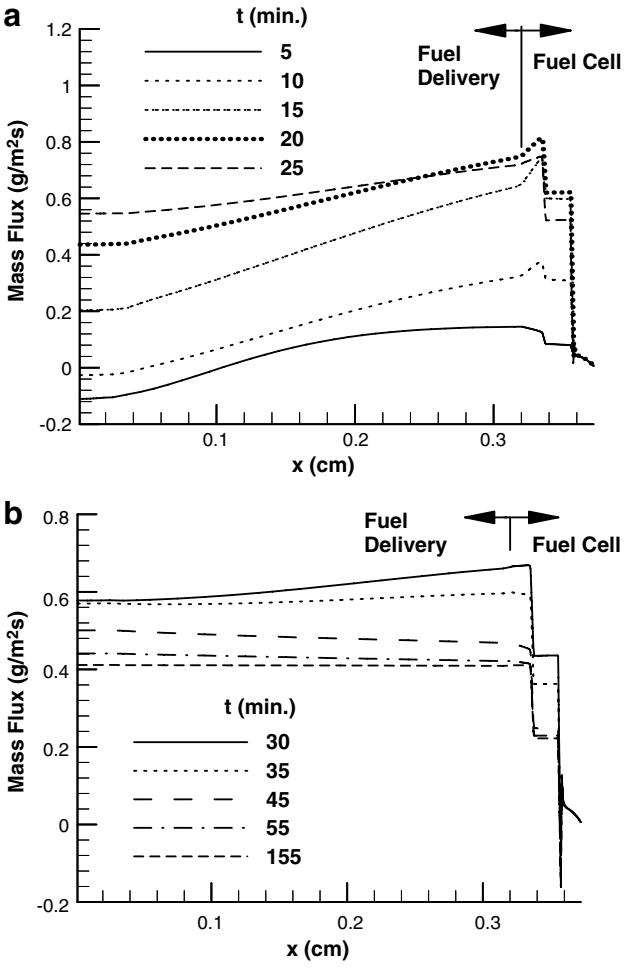

Fig. 13. Area averaged liquid mass flux and vs. distance through the fuel delivery system and fuel cell at (a) early time and (b) later times with a non-preferential wicking length of 3 mm, cell area of 1 cm^2 and $R_\Omega = 1\ \Omega$ at cell temperature of 300 K.

imately zero. This occurs because the liquid is evaporated, and only leaves the system as a vapor. The water produced by the reduction reaction back diffuses through the membrane and is consumed at the 'acl' by the oxidation reaction.

The area averaged mass flux of the gas phase for the entire system, and a zoomed image of the 'ccl' and 'cgdl' is presented in Figs. 14a and b, respectively. The gas produced by chemical reaction in the 'acl' leaves through the 'agdl', because there is too much resistance in the membrane. The gas flows out and through the sides of the non-preferential wicking region. The magnitude of the gas mass flux decreases as the mass flow out of the system in the delivery system. The magnitude of the gas mass flux over time is proportional to the cell-current density over time on the anode side of the fuel cell and in the delivery system. In the 'ccl' and 'cgdl' the vapor mass flux is initially positive, but quickly becomes negative as oxygen is needed during for the reduction reaction at the 'ccl'. However, as time increases, there is methanol cross-over, and carbon

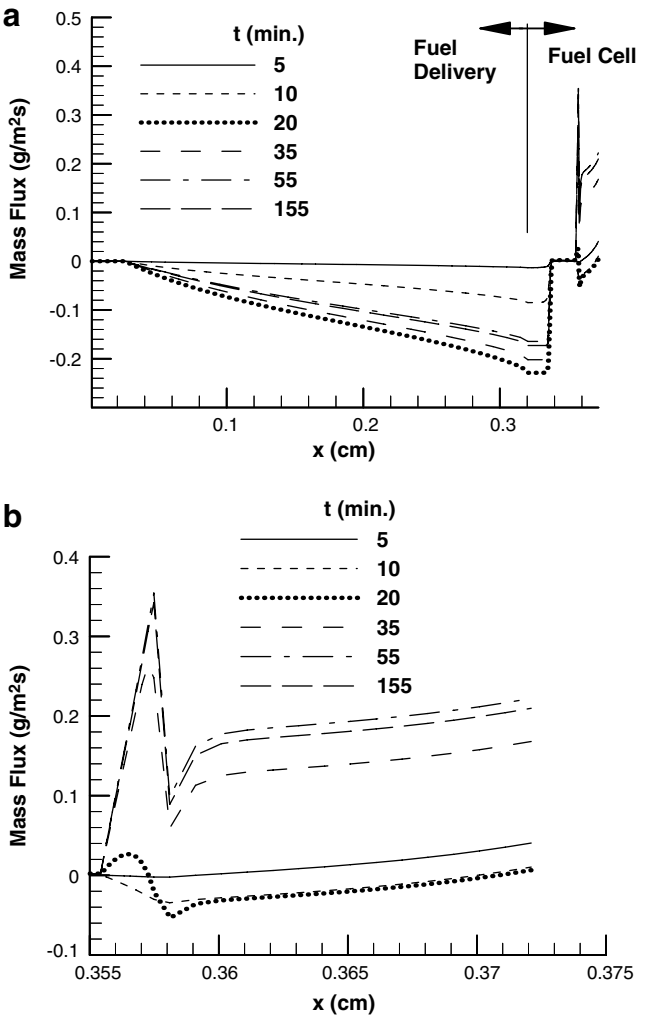

Fig. 14. Area averaged gas mass flux and vs. distance through (a) the fuel delivery system and fuel cell and in the (b) the 'ccl' and 'cgdl' at different times with a non-preferential wicking length of 3 mm, cell area of 1 cm^2 and $R_\Omega = 1\ \Omega$ at cell temperature of 300 K.

dioxide is produced. Also, as the methanol concentration increases, so does the evaporation rate, therefore the gas flux is positive. The sharp changes in mass flux in the 'ccl' correspond to the location where the reduction reaction (oxygen consumption) is the greatest.

4. Conclusions

A numerical model was successfully developed to model the multiphase, transient characteristics of a fuel cell and a passive fuel delivery system. The fuel cell polarization characteristics were analyzed in order to find the optimal operating range in which the fuel cell should run. It was found that much tighter criteria for methanol feed concentration and cell voltage is needed when considering the maximum cell power density with the fuel consumption efficiency than without it. Also it was found that most of the fuel loss is due to evaporation, therefore for significant improvement on the fuel consumption efficiency, a passive system that recaptures the evaporated fuel or limits the evaporation rate is needed.

The proposed passive fuel delivery system was shown to be a successful design in which the fuel can be stored as a pure fuel, and no make-up water was required. With this design, the length of the non-preferential wicking section effects both the start-up time and the cross-over rate in a competing fashion; the shorter the delivery system is, the faster the start-up time, but there will be greater cross-over rates. Further investigations need to be performed to optimize this system. Also, since evaporation rates, diffusion coefficients, and reaction rates are all dependent on temperature, further investigations need to be performed to characterize the thermal effects.

Acknowledgement

This research was funded by the agreement with US Army Communications-Electronics Command (CECOM) under Agreement No. DAAB07-03-3-K-415.

References

[1] A. Faghri, Z. Guo, Challenges and opportunities of thermal management issues related to fuel cell technology and modeling, Int. J. Heat Mass Transfer 48 (2005) 3891–3920.
[2] J.P. Meyers, J. Newman, Simulation of the direct methanol fuel cell, parts I–III, J. Electrochem. Soc. 149 (6) (2002) A718.
[3] B.L. Garcìa, V.A. Sethuran, J.W. Weidner, R.E. White, R. Dougal, Mathematical model of direct methanol fuel cell, J. Fuel Cell Sci. Technol. 1 (2004) 43.
[4] X. Ren, T.E. Springer, A. Zawodzinski, S. Gottesfeld, Methanol transport through nafion membranes, electro-osmotic drag effects on potential step measurements, J. Electrochem. Soc. 147 (2) (2000) 466.
[5] A.A. Kulikovsky, Analytical model of the anode side of DMFC: the effect of non-Tafel kinetics on cell performance, Electrochem. Commun. 5 (2003) 530.
[6] K.T. Jeng, C.W. Chen, Modeling and simulation of a direct methanol fuel cell anode, J. Power Sources 112 (2002) 367.
[7] A.A. Kulikovsky, Two-dimensional simulation of direct methanol fuel cell, a new (embedded) type of current collector, J. Appl. Elecrochem. 30 (2000) 1005.
[8] A.A. Kulikovsky, J. Dvisek, A.A. Kornyshev, Two-dimensional simulation of direct methanol fuel cell, a new (embedded) type of current collector, J. Electrochem. Soc. 147 (3) (2000) 953.
[9] Z.H. Wang, C.Y. Wang, Mathematical modeling of liquid-feed direct methanol fuel cells, J. Electrochem. Soc. 150 (4) (2003) A508.
[10] J.H. Nam, M. Kaviany, Effective diffusivity and water-saturation distribution in single- and two-layer PEMFC diffusion medium, Int. J. Heat Mass Transfer 46 (2003) 4595–4611.
[11] U. Pasaogullari, C.Y. Wang, Two-phase transport and the role of micro-porous layer in polymer electrolyte fuel cells, Electrochim. Acta 49 (2004) 4359.
[12] D. Natarajan, T.V. Nguyen, A two-dimensional, two-phase, multicomponent, transient model for the cathode of a proton exchange membrane fuel cell using conventional gas distributors, J. Electrochem. Soc. 148 (12) (2001) A1324.
[13] A. Faghri, Z. Guo, Thermal Fluids Management for Direct Methanol Fuel Cells, US Patent Office, Patent Pending, 2005.
[14] A. Faghri, Z. Guo, Planar Fuel Cell Stack and Method of Fabrication of the Same, US Patent Office, Patent Pending, 2005.
[15] Z. Guo, A. Faghri, Miniature DMFCs with passive thermal-fluids management systems, J. Power Sources, in press.

[16] Z. Guo, A. Faghri, Development of planar air breathing direct methanol fuel cell stacks, J. Power Sources, in press.
[17] D.R. Lide (Ed.), Handbook of Chemistry and Physics, 85th ed., CRC Press, USA, 2004.
[18] C.L. Yaws, Handbook of Transport Property Data: Viscosity, Thermal Conductivity and Diffusion Coefficients of Liquids and Gases, Gulf Pub. Co., Houston, Tex, 1995.
[19] C.L. Yaws, Thermodynamic and Physical Property Data, Gulf Pub. Co., Houston, Tex, 1992.
[20] F.P. Incropera, D.P. Dewitt, Fundamental of Heat and Mass Transfer, 5th ed., John Wiley & Sons, USA, 2002.
[21] A. Faghri, Heat Pipe Science and Technology, Tayor & Francis, USA, 1995.